PAPER

Check for updates

Tailoring a hierarchical porous carbon electrode from carbon black *via* 3D diatomite morphology control for enhanced electrochemical performance†

Eugene Sefa Appiah, [ID] *[ab] Kwadwo Mensah-Darkwa,*[ac] Anthony Andrews,[a] Frank Ofori Agyemang,[a] Martinson Addo Nartey, [ID] [a] Katlego Makgopa,[d] Yongdan Hou,*[ef] Patrick Aggrey [ID] [g] and David Ato Quansah[h]

Carbon black, a nano-porous material usually derived from the pyrolysis of waste tyres possesses varied particle sizes and morphology making it a viable material for several engineering applications. However, the high tendency for CB to agglomerate remains a challenge. To address this, bio-templating has been employed to produce a nanostructured porous carbon electrode material for supercapacitor applications using diatomite as a template. Diatomite-synthesized activated carbon (DSAC) was fabricated through a three-step process involving acid treatment of diatomite, thermal activation of carbon black, and bio-template synthesis. The resulting material was thoroughly characterized using XRD, Raman spectroscopy, BET analysis, and SEM imaging. Its electrochemical properties were assessed through cyclic voltammetry, galvanostatic charge–discharge, and electrochemical impedance spectroscopy. The DSAC material exhibited a high specific surface area of 266.867 m^2 g^{-1}, pore volume of 0.6606 cm^3 g^{-1}, and mean pore radius of 1.8943 nm. The electrochemical evaluation revealed that DSAC demonstrates excellent electrochemical performance, achieving a high specific capacitance of 630.18 F g^{-1} and retaining 94.29% capacitance after 5000 cycles at 1 A g^{-1}. The DSAC electrode is eco-friendly and a promising candidate for supercapacitor applications.

1 Introduction

In recent years, the energy demand has risen sharply due to rising population and industrialization. To address these global energy and environmental needs, modern scientific research has focused on developing renewable energy systems like wind and solar power.[1,2] Despite the significant progress made in solar and wind power generation, intermittent energy production due to weather and location remains a major challenge.[3] Therefore, efficiently utilizing such energy sources requires energy storage devices for power transfer.[4–6] Supercapacitors, known for their high power densities, rapid charge/discharge rates, long cycle life, and environmental friendliness are widely used in electronic devices, electric vehicles, and power stations[7–10] where the energy storage capacity of supercapacitor cells relies heavily on the electrode materials.[2,11–13] These electrode materials can be classified into electric double layer capacitors and pseudocapacitors comprising carbon-based materials and conducting polymers/metal oxides respectively. An electric double layer capacitor (EDLC) has high specific surface area, high specific capacitance, and high-power density while pseudocapacitors possess high energy density and a fast charge and discharge rate. Currently, carbon-based materials usually classified as EDLCs are predominantly used as electrode materials for supercapacitor application due to their characteristics. Carbon based electrode materials offer a theoretical specific capacitance of 100–200 F g^{-1}.[14,15] Despite their relatively

aDepartment of Materials Engineering, College of Engineering, Kwame Nkrumah University of Science and Technology, Kumasi, Ghana. E-mail: anthonydrews@gmail.com; foagyemang88@gmail.com; maddonartey@knust.edu.gh

bDepartment of Sustainable Mineral Resource Development, University of Energy and Natural Resources, Sunyani, Ghana. E-mail: appiaheugenesefa@gmail.com

cThe Brew-Hammond Energy Centre, Kwame Nkrumah University of Science and Technology (KNUST), Kumasi, Ghana. E-mail: kmdarkwa.coe@knust.edu.gh

dDepartment of Chemistry, Faculty of Science, Tshwane University of Technology, Pretoria, South Africa. E-mail: Makgopak@tutac.za

eHubei Key Laboratory of Energy Storage and Power Battery, School of Materials Science and Engineering, Hubei University of Automotive Technology, Shiyan, China. E-mail: yongdan.hou@huat.edu.cn

fShiyan Industrial Technology Research Institute of Chinese Academy of Engineering, Shiyan, China

gHierarchically Structured Materials Laboratory, Skolkovo Institute of Science and Technology, 121205 Moscow, Russia. E-mail: Patrick.aggrey@skoltech.ru

hDepartment of Mechanical Engineering, College of Engineering, Kwame Nkrumah University of Science and Technology, Kumasi, Ghana. E-mail: daquansah.coe@knust.edu.gh

† Electronic supplementary information (ESI) available. See DOI: https://doi.org/10.1039/d4na00680a

high theoretical specific capacitance values, carbon-based electrode materials for supercapacitor applications fall short in meeting the fast-paced demands of electric device advancements.[16] Carbon black used as a carbon-based electrode material has exhibited a theoretical specific capacitance of 100–120 F g^{-1} in the literature which is relatively lower than values reported for other carbon-based electrode materials.[17–19] Such a low theoretical specific capacitance value most likely results from a smaller specific surface area, pore volume, or less definite pore structure due to particle agglomeration of carbon black compared to other carbon-based electrode materials.[20–22] Despite this drawback, carbon black has been widely considered in supercapacitor applications due to its cost-effectiveness, electrical conductivity, and availability.[17,23,24] Nasibi et al.,[18] prepared nano-iron oxide (Fe_2O_3)/carbon black electrodes for electrochemical capacitors using a mechanical pressing method in a 2 M KCl electrolyte. It was revealed in their study that after 500 cycles at 20 mV s^{-1}, the electrodes showed a specific capacitance of 40.07 F g^{-1} for the 30 : 60 : 10 (carbon black: Fe_2O_3: polytetrafluoroethylene) mix, retaining a capacitance of 80%. Also, Chen et al.,[19] used nitrogen-functionalized carbon black from waste tires, coactivated with melamine and alkali agents like $C_4H_6K_2O_7$–M. $C_4H_6K_2O_7$–M exhibited a higher capacitance and surface area of 48 F g^{-1} and 247.5 m^2 g^{-1} respectively than commercial carbon black (0–40 F g^{-1}) with a similar surface area (300 m^2 g^{-1}). Through this approach, the surface area, pore structure, and conductivity were enhanced and resulted in an improved electrochemical performance. In an attempt to significantly improve the electrochemical performance of carbon black as a supercapacitor electrode, recent attention has focused on synthesis methods of the electrode.[25–27] Currently, the templating method has received much attention due to its merits including controlled structure, reproducibility, cost-effectiveness, versatility, eco-friendliness, and safety.[27–29] Depending on the material used, template synthesis can be classified into the bio-template method,[30] hard template method,[28,31] soft template method,[13] and hybrid template method.[32] Among the various template methods, bio-templating is often preferred because of its cost-effectiveness, eco-friendliness and its ability to produce complex structures.[30,33] Diatomite, a naturally occurring sedimentary rock mainly made of amorphous silica, has recently been used as a bio-template for electrode material synthesis due to its hierarchical nanoporous network structures.[34–37] Diatomite's natural hierarchical structure, high surface area, and biocompatibility make it an ideal template for creating interconnected pores, which significantly improve ion transport and enhance the electrochemical performance of the carbon electrodes.[38,39] Y. Huang et al. (2021)[40] described the fabrication of N-doped porous carbon (NPC) by thermally treating waste diatomite at high temperatures with a bulk of yeast protein that had been adsorbed during beer filtration. The NPC-2 electrode material exhibited a specific capacitance of 151.5 F g^{-1} at 1 A g^{-1}, with a notable capacitance retention of 90.5% after 10 000 cycles. The symmetric supercapacitor using NPC-2 achieved an energy density of 13.47 Wh kg^{-1} at a power density of 400 W kg^{-1}. Yang et al.[37] used diatomite to produce a MoS_2/amorphous carbon

composite electrode, achieving a capacitance of 167.3 F g^{-1} and 93.2% retention after 1000 cycles owing to the unique structure and interaction between MoS_2 and amorphous carbon. Guo et al.,[41] fabricated a 3D composite for supercapacitors from hollow diatomite silica coated with TiO_2 and MnO_2 (diatomite@TiO_2@MnO_2). Here, the added TiO_2 layer improved performance, with good cycling stability (94.1% retention after 2000 cycles) and high efficiency (98.2–99.6% retention). By using low-cost natural diatomite and a scalable process, the diatomite@TiO_2@MnO_2 electrode showed promise for energy storage applications.[41] Therefore, this study enhances energy storage by controlling the morphology of carbon black with diatomite as a template. Using carbon black aims to develop a cost-effective and green energy storage solution. Ultimately, the study explores hierarchical porous carbon from carbon black for potential use in supercapacitor electrodes, contributing to a cleaner energy future.

2 Experimental details

2.1. Materials

The carbon black used was obtained from Alchemy Alternative Energy Company in Prampram, Accra, Ghana, while the diatomaceous earth powder with a specific composition of SiO_2 (86%), Na_2O (0.22%), K_2O (1.39%), Al_2O_3 (5.5%), MgO (0.78%), and Fe_2O_3 (2.5%) was purchased from Kyrkyma.ru. The nickel foam current collector, hydrochloric acid (HCl, 37%), sodium hydroxide (NaOH, 97%), and potassium hydroxide (KOH, 85%) pellets were procured from Sigma-Aldrich (St. Louis, MO, USA). All analytical grade chemicals were used as obtained.

2.2. Materials preparation

The diatomite-synthesized activated carbon was obtained using an acid treatment and a three-step high-temperature treatment method. First, the diatomite powder (5 g) was purified through acid treatment and rinsed with deionized water to remove pore-blocking impurities. The diatomite was mixed with 50 mL of deionized water and stirred for 30 minutes. Afterward, 50 mL hydrochloric acid solution (1 M HCl) was added dropwise into the mixture and stirred for 3 hours. The resulting acid-treated diatomite (ATD) was filtered and washed with deionized water until a neutral pH of 7 was reached. Additional purification was carried out by subjecting the ATD to an initial heating process at 250 °C for 2 hours, at a heating rate of 5 °C min^{-1}. This step aimed to eliminate any impurities and residual organic materials. Carbon black (CB) was activated at 800 °C for 3 hours in a furnace atmosphere. Afterward, the pre-heated acid-treated diatomite powder was mixed with the activated carbon black in a mass ratio of 1 : 3, after a series of preliminary studies on the weight ratios. The mixture was stirred at 300 rpm for 2 hours and then subjected to hydrothermal heat treatment at 160 °C in a stainless-steel autoclave for 12 hours. The hydrothermally treated mixture was rinsed in 5 mol L^{-1} NaOH solution to etch out the diatomite leaving behind the intricate 3D network structure within the material. The following reactions occurred, primarily between the silica and the NaOH solution. Thus, the

silica (SiO_2) will dissolve to form sodium silicate as observed in eqn (1):

$$\text{Primary reaction: } SiO_2 + 2NaOH \rightarrow Na_2SiO_3 + H_2O \qquad (1)$$

However, the possible side reactions that occurred due to the specific composition of diatomite (SiO_2 (86%), Na_2O (0.22%), K_2O (1.39%), Al_2O_3 (5.5%), MgO (0.78%), and Fe_2O_3 (2.5%)) include:

(1) Aluminosilicate formation: Al_2O_3 in diatomite could react with NaOH and dissolved silica, forming sodium aluminosilicate as shown in eqn (2).

$$Al_2O_3 + 2SiO_2 + 4NaOH \rightarrow Na_4Al_2Si_2O_9 + 2H_2O \qquad (2)$$
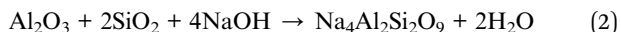
(2) Iron oxides (Fe_2O_3): iron oxide may precipitate as $Fe(OH)_3$ or remain in the solution as a hydroxide complex, depending on reaction conditions.

$$Fe_2O_3 + 6NaOH \rightarrow 2Fe(OH)_3 + 3Na_2O \qquad (3)$$

(3) Magnesium oxide (MgO): MgO will form magnesium hydroxide:

$$MgO + H_2O \rightarrow Mg(OH)_2 \qquad (4)$$

The small amounts of Na_2O and K_2O might remain in the solution as Na^+ and K^+ ions and could contribute to further ionic interactions but are unlikely to drive major side reactions. The main outcome is the dissolution of silica with the potential formation of aluminosilicates and hydroxides of iron and magnesium.

Thus, the diatomite bio-template synthesis method produced a nanostructured porous carbon (diatomite synthesized activated carbon (DSAC)) after drying at 105 °C for 12 hours followed by deionized water washing. Fig. 1 illustrates the steps involved in preparing the DSAC as an electrode material.

2.3. Electrode preparation

The electrodes were prepared by grinding and sieving the electrode materials/active material, namely carbon black (CB), activated carbon black (ACB), acid-treated diatomite (ATD), and diatomite synthesized activated carbon (DSAC) into a fine powder using a 90-micron sieve. A mixture of 4 mg of electrode/active materials (CB, ACB, ATD, and DSAC), along with the binder (polyvinylidene fluoride – PVDF) and organic solvent (dimethylformamide – DMF), was coated on the nickel (Ni) foam current collector using a ductile blade at a ratio of 0.9 : 0.07 : 0.03, respectively. The coated electrode materials (CB, ACB, ATD, and DSAC) were dried at 80 °C for 12 hours. Finally, the fabricated electrodes (CB, ACB, ATD, and DSAC) were assessed for their electrochemical performance.

2.4. Materials characterization

Fourier transmission infrared (FTIR) spectroscopy analysis was carried out using a PerkinElmer 2000 FTIR spectrometer with Spectra 10™ software (PerkinElmer, Norwalk, USA) at room temperature (25 °C). The absorption spectra were recorded in the range of 500 to 4000 cm^{-1}. UV-vis analysis was conducted using a Lambda 365 UV-vis spectrophotometer operated at a wavelength of 200–1100 nm. DMF was used to evaluate the electronic properties of the prepared materials. X-ray diffraction (XRD) was performed on a D8-Discover Bruker X-ray diffractometer with Cu K radiation ($\lambda = 1.540$ Å). Raman spectroscopy analysis for the electrodes was carried out with high-resolution Raman (HR Raman) spectroscopy (Morphologi 4-ID Raman Spectrometer) using an argon ion laser (514 nm) to investigate the graphitization order. UH-resolution SEM was conducted *via* an in-beam SE scan mode using a Tescan Magna SEM. X-ray microanalyses were performed to evaluate the elemental composition of the electrodes using the energy-dispersive X-ray microanalyzer attachment of the Tescan Magna SEM. Nitrogen desorption studies were carried out at 77.35 K using a NOVA Touch 2LX (Quantachrome TouchWin version 1.21, Quantachrome instruments), with surface area evaluated using the Brunnauer–Emmett–Teller (BET) model. Approximately 0.2246 g of dry particles are outgassed for approximately 574.25 min at 30.1027 °C. The Barrett–Joyner–Halenda (BJH) technique was used to calculate the pore-size distribution from the desorption branch of the isotherms.

2.5. Electrochemical evaluation

A three-electrode setup was used, with a silver/silver chloride reference electrode, a graphite rod counter electrode, and active
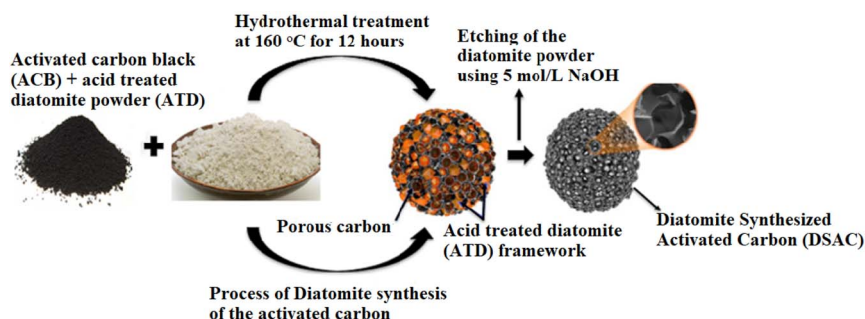

Fig. 1 Diagram illustrating the formation of diatomite synthesized activated carbon (DSAC). This figure has been adapted/reproduced from ref. 42 with permission from Elsevier, copyright 2018.

Table 1 The elemental composition (wt%) of the CB, ACB, and DSAC samples using energy dispersive X-ray (EDX)

Elements	C	O	Na	Mg	Al	Si	S	Cl	K	Ti	Fe	Cu	Zn
CB	85.3	13.2	0.00	0.0	0.07	0.91	0.27	0.03	0.0	0.09	0.0	0.11	0.18
ACB	64.9	24.0	0.24	0.0	0.19	1.23	0.37	0.10	0.0	8.12	0.0	0.17	0.58
DSAC	65.3	28.7	0.12	0.09	0.59	3.46	0.06	0.04	0.8	0.05	0.22	0.12	0.31

material (*i.e.*, CB, ACB, ATD, and DSAC) as the working electrode where Ni foam was used as a current collector. The electrode materials, weighing 4 mg and spanning 0.65 cm^2, were tested electrochemically at room temperature in a 6 M KOH aqueous solution using a CORRTEST Workstation. Cyclic voltammetry (CV) was performed by scanning at rates of 1, 10, 50, and 100 mV s^{-1} at a constant voltage within the range of -1 to 0 V. Galvanostatic charge and discharge cycles were conducted at current densities of 0.25, 0.5, 1, and 2.5 A g^{-1} within the same voltage window. The cycling stability test at was performed at a constant current density of 1 A g^{-1} for 5000 cycles. The specific capacitance values were determined for CV analysis and galvanostatic charge/discharge cycles using eqn (1) and (2).[43,44]

$$C_s = \frac{A}{m\left(\dfrac{V}{t}\right)(v_2 - v_1)} \quad (5)$$

C_s which represents the specific capacitance was calculated as the ratio of the integral area (A) to the product of electrode mass (m), scan rate (V/t), and voltage window ($v_2 - v_1$).

$$C_s = \frac{I}{m\,\mathrm{d}V/\mathrm{d}t} \quad (6)$$

C_s represents specific capacitance, calculated as the ratio of the product of current density (i) and change in discharge time ($\mathrm{d}t$) to the change in the voltage (voltage window ($\mathrm{d}V$)), and i represents current density and it is mathematically expressed as $\frac{I}{m} = i$, which is the ratio of the current to the mass of the electrode.

Energy and power density values were assessed using various mathematical relations, including eqn (3) and (4) for energy density and eqn (5) and (6) for power density.[45–47]

$$E = \frac{C_s V^2}{2} \quad (7)$$

$$E = \frac{C_s V^2}{2 \times 3.6} \quad (8)$$

E represents energy density, C_s is the specific capacitance, and V^2 denotes the voltage window.

$$P = \frac{V^2}{4R_s} \quad (9)$$

P denotes the power density, V^2 signifies the voltage window, and R_s represents the internal series resistance.

$$P = \frac{E \times 3600}{\Delta t} \quad (10)$$

P represents power density, E implies energy density, and Δt signifies the change in discharge time.

Furthermore, we performed electrochemical impedance spectroscopy analysis, ranging from 100 kHz to 0.01 Hz.

3 Results and discussion

3.1. Physical and chemical characterization

Table 1 displays the elemental compositions of the synthesized samples: CB, ACB, and DSAC. From Table 1, the CB, ACB, and DSAC samples recorded a high weight percent of carbon with DSAC recording the highest. However, graphite and graphitic nature of the CB, ACB, and DSAC is not entirely pure, as they coexist with other elements such as C, O, Na, Mg, Al, Si, S, Cl, K, Ti, Fe, Cu, and Zn as observed in Table 1. The DSAC electrode material recorded an increase in the composition of Al, Si, and K relative to its weight percentages for CB and ACB because of residual element traces from the diatomite bio-template synthesis of the DSAC material. The increase in oxygen atoms can be attributed to graphite oxidation, facilitated by the role of KOH as a reducing agent as observed in Table 1. The weight percentage of silicon in the DSAC sample demonstrates the successful removal of almost all the silica templates through the sodium hydroxide etching method.

Fig. 2 shows the FTIR spectra of the CB, ACB, ATD, and DSAC samples. From the spectra, CB, ACB, and DSAC showed a very weak C–C stretching at 1735 cm^{-1}, with CB and ACB showing an extra weak C–H aromatic functional group at 1075 cm^{-1}. ACB displays a weak C–H stretching at 1372 cm^{-1} (ref. 23). Also, CB, ACB, and DSAC revealed a C–H aromatic group at 2950 cm^{-1} as observed in ESI Fig. S1.† The ATD sample which is a silica based material reveals Si–O–Si and Si–O–Al functional groups at 1050
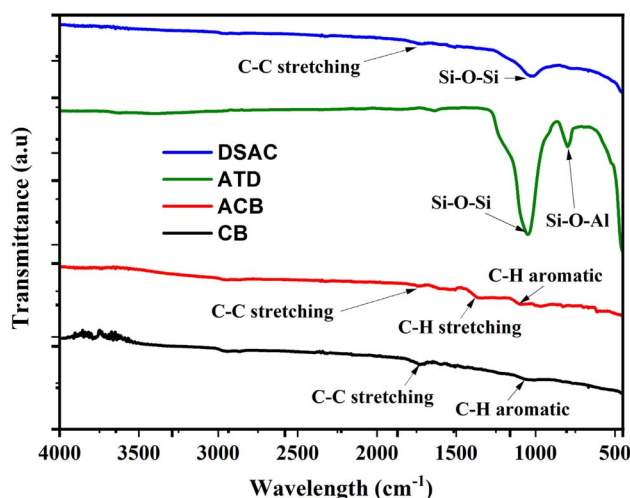
Fig. 2 Fourier transmission infrared transmittance of CB, ACB, ATD, and DSAC samples.

and 800 cm^{-1} respectively. In DSAC, traces of silicon in ATD were observed as shown in Table 1 leading to a peak of a Si–O–Si functional group in the DSAC spectra which was revealed at 1025 cm^{-1}.[48] The Si–O–Si functional group observed in DSAC led to a shift in the peak of the Si–O–Si functional group of ATD from a wavenumber of 1050 to 1025 cm^{-1} in the DSAC spectra.

The UV-vis absorption spectra of the CB, ACB, ATD, and DSAC samples with a zoomed-in section are displayed in ESI Fig. S2.† Fig. 3 displays the XRD patterns of CB, ACB, ATD, and DSAC samples. Two separate diffraction peaks that conform to the (0 0 2) and (1 0 0) lattice planes of graphitic carbon were identified at 25° and 44° for the CB and DSAC samples. Also, the CB sample exhibited (1 1 1), (2 2 0), and (3 1 1) peaks due to the presence of silicon. However, the ACB sample shows no peaks, which signifies a low degree of graphitization. The ATD sample recorded (1 0 0), (1 1 0), and (1 1 3) silicon peaks at an angle of 22°, 36° and 63° respectively. However, the DSAC sample exhibits a broader and less intense (0 0 2) peak at 25°which confirms a change in the crystal structure due to bio-templating and subsequently increases defects and pores while reducing the ordered nature of carbon.

The Raman spectra of CB, ACB, and DSAC samples reveal distinct D-band and G-band characteristics at specific wavenumbers (see Fig. 4). D-band peaks were observed at 1338 cm^{-1}, 1347 cm^{-1}, and 1342 cm^{-1} while G-band peaks were found at 1590 cm^{-1}, 1577 cm^{-1}, and 1573 cm^{-1}. The D and G bands are prominent in all spectra except for the ATD sample. ACB and DSAC spectra exhibit similar intensities for D and G bands whiles the CB sample showed a slightly higher G-band intensity. The Raman spectra of CB, ACB, DSAC align with those of materials with sp^2-linked carbons according to M. Boota *et. al.*[49] The I_D/I_G ratios for CB, ACB, and DSAC were 0.936, 1.015, and 1.008, respectively. The nearly equal unity values indicate a well-balanced presence of disordered or amorphous carbon and graphite (degree of graphitization) in all samples.[50,51]

Fig. 5 shows the adsorption/desorption isotherms for the samples, namely CB, ACB and DSAC revealing its porosity in a relative pressure range of 0 to 1.0. At relatively low pressure (P/

Fig. 4 Raman spectra of the CB, ACB, ATD and DSAC samples.

Fig. 5 A plot of the volume adsorbed/desorbed isotherm for the CB, ACB, ATD and DSAC samples against the relative pressure and an inset of the BET plot of all the samples, namely CB, ACB, ATD, and DSAC.

P_0), the N$_2$ adsorbed volume increased sharply with the relative pressure, which can be attributed to the filling of the micropores with N$_2$.[52] The mean pore radius, pore volume, and specific surface area for CB, ACB, DSAC, and ATD are summarized in Table 2. The pore radius values show the existence of mesopores from the porous network structure of DSAC, and
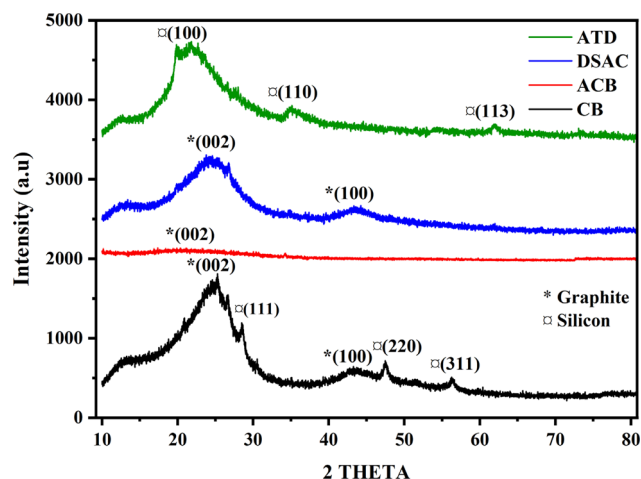

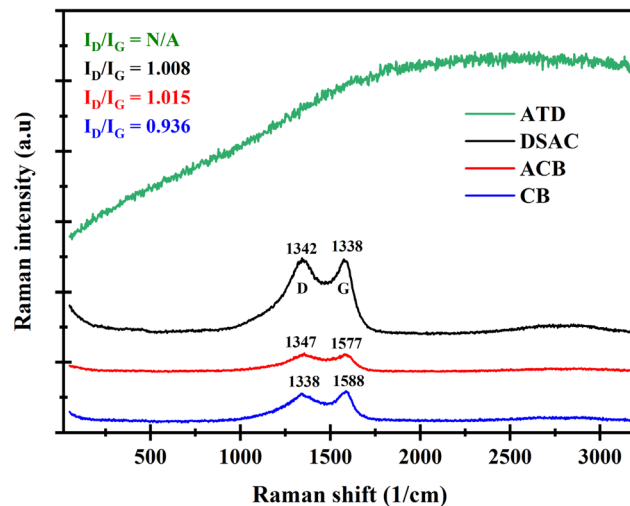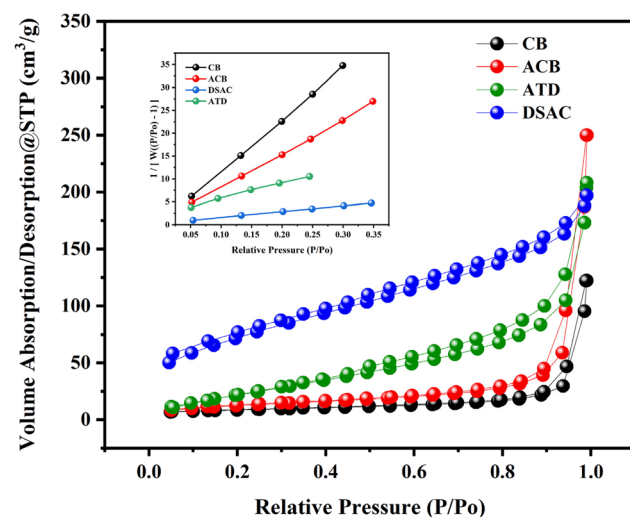**Fig. 3** X-ray diffraction analysis of the CB, ACB, ATD, and DSAC samples.

Table 2 Tabulation of the surface area values using the BET model and the pore radius, and pore volume values using the BJH analysis model

| Samples	Surface area	Pore volume	Pore radius d$V(r)$
CB	30.3661 m^2 g^{-1}	0.1826 cm^3 g^{-1}	14.174 nm
ACB	46.6212 m^2 g^{-1}	0.3815 cm^3 g^{-1}	1.9101 nm
ATD	94.9455 m^2 g^{-1}	0.3066 cm^3 g^{-1}	1.6944 nm
DSAC	266.867 m^2 g^{-1}	0.6606 cm^3 g^{-1}	1.8944 nm

Table 3 Comparison of the surface area, pore size and volume of the DSAC electrode material with template–assisted electrode materials in the literature

Sample	Synthesis method	Surface area	Pore volume	Pore size/radius	Ref.
N-doped carbon	Zeolite-templating route	$1529 \ m^2 \ g^{-1}$	$0.75 \ cm^3 \ g^{-1}$	1.96 nm	53
Diatomite waste-derived N-doped porous carbon	Diatomite template assisted	$754 \ m^2 \ g^{-1}$		7.216 nm	40
MoS_2/amorphous carbon composite	Diatomite template assisted	$361.6 \ m^2 \ g^{-1}$	$0.621 \ cm^3 \ g^{-1}$	5.1 nm	37
NiFeS$_x$@CNTs@MnS@Diatomite electrode	CVD on a diatomite substrate and the two-step hydrothermal method	$62.3 \ m^2 \ g^{-1}$		4.0 nm	54
DSAC	Diatomite assisted template	$266.867 \ m^2 \ g^{-1}$	$0.6606 \ cm^3 \ g^{-1}$	1.8944 nm	This work

activation of carbon black and macropores in the carbon black sample. This can also be confirmed from the isotherms of all the samples observed in Fig. 5. The DSAC sample exhibits a uniform pore size distribution which confirms the synthesis of a hierarchical porous structure[40] resulting in a type II isotherm (see Fig. 5). DSAC exhibits superior N_2 gas adsorption compared to ACB, CB, and ATD which showed a type III isotherm. This is reflected in the high specific surface area ($266.867 \ m^2 \ g^{-1}$), pore volume ($0.6606 \ cm^3 \ g^{-1}$), and mean pore radius (1.8944 nm) of DSAC (see Table 2). The inset shows that the steeper the slope of the BET surface area plot, the smaller

the surface area of the sample which can be confirmed in Table 2 with the DSAC sample having the highest surface area value for both the BET and BJH models. The DSAC electrode material was compared with template-assisted electrode materials in the literature as shown in Table 3. The comparison shows that DSAC had a relatively lower surface area but higher pore volume and relatively smaller pore sizes.

Fig. 6(a)–(d) depict SEM images of all the electrode materials (ATD, CB, ACB, and DSAC). Fig. 6(a) shows the hierarchically porous structure of the ATD sample while Fig. 6(b) and (c) show agglomeration of carbon particles with interconnected micro
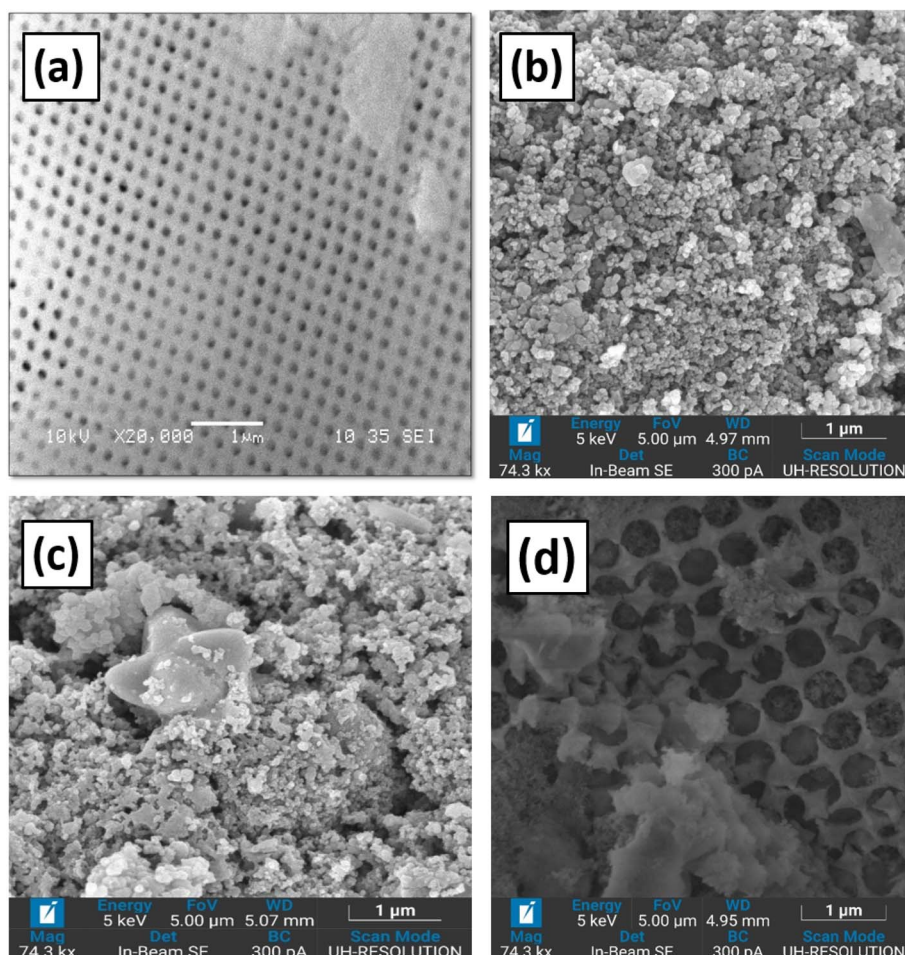
Fig. 6 Scanning electron microscopy images of the ATD, CB, ACB, and DSAC samples labeled as (a), (b), (c), and (d), respectively.

and mesopores upon activating the CB sample, respectively. The DSAC material replicated the morphology of diatomite (see Fig. 6(a) and (d)). Moreover, the DSAC and ACB structures exhibit distinct properties, with the former displaying

nanoflower-like structures inside its pore network and the latter exhibiting highly dense agglomerated carbon particles. The obtained DSAC has a 3D hierarchical pore structure as shown in Fig. 6(d) with a pore radius of approximately 1.8944 nm
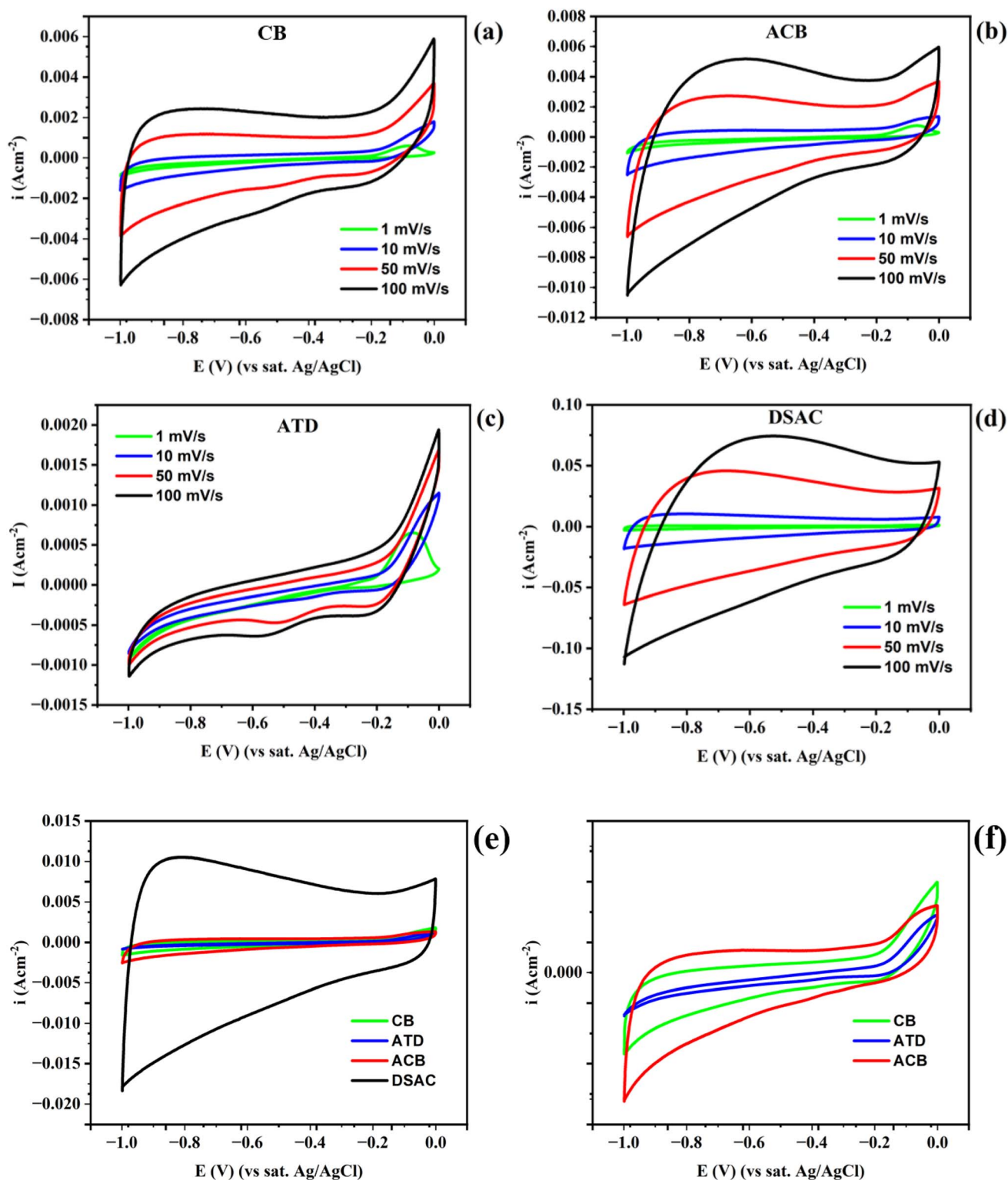

Fig. 7 Cyclic voltammetry curves for (a) CB, (b) ATD, (c) ACB, and (d) DSAC at scan rates of 1, 10, 50, and 100 mV s⁻¹ within a voltage range of −1 to 0. (e) Overlaid plots for all the electrode materials at a scan rate of 1 mV s⁻¹ within a voltage range of −1 to 0 and (f) expanded version of the combined plot labelled (e) without DSAC.

compared to ATD with a pore radius of 1.6944 nm. Meanwhile, CB and ACB have pore radii of 14.1738 nm, and 1.9101 nm respectively as observed in Table 2. These findings indicate the porous nature and nanoscale properties of the materials. Upon removal of the SiO_2 core, DSAC replicated the porous network structure of ATD. Hence, activating, and synthesizing nanoporous carbon through the diatomite template-assisted method leads to an increase in pore volume and surface area values.

3.2. Electrochemical measurements

Fig. 7(a)–(d) show the cyclic voltammetry curves of CB, ACB, ATD, and DSAC samples at scan rates of 1, 10, 50, and 100 mV s^{-1} within a voltage window of −1 to 1, while Fig. 7(e) and (f) show the overlaid plots of cyclic voltammetry (CV) curves for CB, ACB, ATD, and DSAC samples, along with the expanded version of Fig. 7(e) excluding DSAC. Notably CV curves for CB, ACB, and DSAC exhibit nearly rectangular shapes with slight distortion, suggesting favorable electrochemical behaviour and rapid
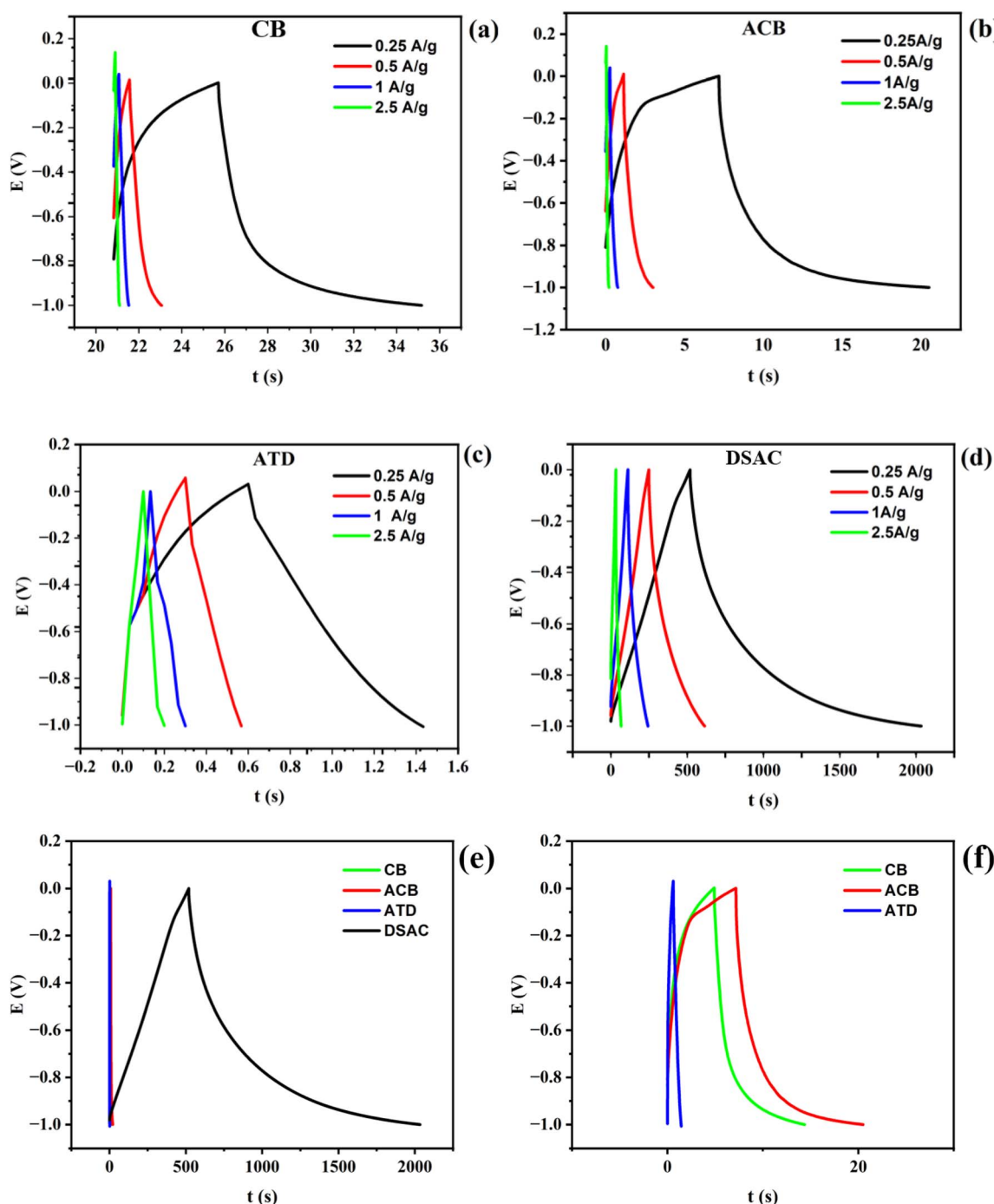

Fig. 8 The galvanostatic charge and discharge cycles of (a) CB, (b) ATD, (c) ACB, and (d) DSAC at scan rates of 0.25 A g^{-1}, 0.5 A g^{-1}, 1 A g^{-1}, and 2.5 A g^{-1} within a voltage range of −1 to 0. (e) Overlaid plots for all the electrode materials at a current density of 0.25 A g^{-1} within a voltage range of −1 to 0 and (f) expanded version of the combined plot labelled (e) without DSAC.

charge propagation. The DSAC electrode material records the highest electrochemical double-layer capacitive performance, characterized by a high current response and large charge separation compared to CB and ACB. Thus, DSAC at lower scan rates showed excellent electrochemical behaviour, which indicates the effective transfer of ions into desirable nanostructures and a controlled pore architecture of the electrode material (refer to Fig. 7(e) and (f)). CV curves for ATD show oxidation and reduction peaks across all scan rates, with prominent redox peaks observed at a scan rate of 1 mV s^{-1}, indicating pseudo-capacitive behaviour. Contrarily, the absence of redox peaks in DSAC (see Fig. 7(d) and (e)) is an indication of strong electrochemical double-layer capacitive charge storage mechanisms in the CV curve of the DSAC electrode arising from the effective etching of the ATD material out of DSAC using 5 mol L^{-1} NaOH as observed in the composition of DSAC in Table 1.

Fig. 8(a)–(d) show the galvanostatic charge and discharge (GCD) cycles of CB, ACB, ATD, and DSAC at scan rates of 0.25 A g^{-1}, 0.5 A g^{-1}, 1 A g^{-1}, and 2.5 A g^{-1} within a voltage window of -1 to 0, while Fig. 8(e) and (f) show an overlaid plot of the galvanostatic charge and discharge (GCD) cycles for CB, ACB, ATD, and DSAC samples, along with the expanded version of Fig. 8(e) excluding DSAC. The GCD curves of CB, ACB, ATD, and DSAC at different current densities displayed a non-symmetric curve for all the samples. From Fig. 8(e), the capacitance which is relative to the discharge time tends to increase as the current density decreases. Thus, the progressively long discharging time of the samples at a lower current density is because at lower current densities a slower rate of scanning ensures the ability of the ions to be stored in the electrode materials (see Fig. 8(e)). The DSAC electrode material displays a superior discharge time compared to CB, ACB, and ATD resulting from the successful replication of the structure of diatomite ensuring its high surface area to store charges.

Tables 4 and 5 display the estimated values for electrochemical properties such as the capacitance, discharge time, specific capacitance, energy densities, and power densities for both CV and GCD analysis at a scan rate and current density of

Table 4 Capacitance, energy, and power densities were obtained from cyclic voltammetry curves at a scan rate of 1 mV s^{-1}

Samples	Capacitance	Specific capacitance (F g^{-1}) eqn (1)	R_s/ESR value	Energy density (Wh kg^{-1}) eqn (3)	Energy density (Wh kg^{-1}) eqn (4)	Power density (W kg^{-1}) eqn (5)
CB	0.07230	18.07	1.28	9.04	2.5	0.195
ATD	0.04684	11.71	0.286	5.86	1.63	0.87
ACB	0.106	26.58	1.68	13.29	3.69	0.148
DSAC	2.52072	630.18	0.377	315.09	87.5	0.66

Table 5 Results from galvanostatic charge and discharge cycles at a current density of 0.25 A g^{-1} include discharge time, specific capacitance values, and energy/power densities

Samples	Discharge time (Δt)	Specific capacitance (F g^{-1}) eqn (1)	Energy density (Wh kg^{-1}) eqn (3)	R_s/ESR value (Ω)	Energy density (Wh kg^{-1}) eqn (4)	Power density (W kg^{-1}) eqn (6)	Power density (W kg^{-1}) eqn (6)
CB	30.17	7.5	3.75	1.28	0.52	447.46	1.23
ATD	1.2	0.3	0.15	0.286	0.020	450	0.047
ACB	42.93	10.73	5.36	1.68	0.74	449.475	1.76
DSAC	1515.4	378.85	189.43	0.377	52.62	450.01	125

Table 6 Comparison of the high-performing electrode material (DSAC electrode) with template-assisted electrode materials in the literature

Electrode material	Synthesis approach	Electrolyte	C_s (F g^{-1}) @ current density/scan rate	Energy density (Wh kg^{-1}) @ power density of W kg^{-1}	Ref.
Diatomite waste derived N-doped porous carbon	Diatomite template assisted method	6 M KOH	151.5 F g^{-1}@1 A g^{-1}	13.47 Wh kg^{-1}@400 W kg^{-1}	40
MoS$_2$/amorphous carbon composite	Diatomite template assisted	—	167.3 F g^{-1}@0.5 A g^{-1}	—	37
NiFeS$_x$@CNTs@MnS@Diatomite electrode	CVD on a diatomite substrate and the two-step hydrothermal method	—	552 F g^{-1}@1 A g^{-1}	28.9 Wh kg^{-1}@9375 W kg^{-1}	54
N-doped carbon	Zeolite-templating route	6M KOH	45.7 F g^{-1}@0.1 A g^{-1}	6.4 Wh kg^{-1}@10$^{2.5}$ W kg^{-1}	53
DSAC electrodes	Diatomite assisted template	6M KOH	630.18 F g^{-1}@1 mV s^{-1} 378.85 F g^{-1}@0.25 A g^{-1}	87.5 Wh kg^{-1}@0.66 W kg^{-1} 52.62 Wh kg^{-1}@125 W kg^{-1}	This work

1 mV s^{-1} and 0.25 A g^{-1} respectively. The electrochemical properties recorded in Tables 4 and 5 for the CV curves and GCD cycles were evaluated using eqn (5)–(10), respectively. The specific capacitance values for the CV curves and GCD cycles for CB, ACB, ATD, and DSAC increased as the scan rates and current densities decreased. Thus, the increase in scan rate and current densities results in the fast kinetics observed at the interface depriving the charges of enough contact time for the electrode/charge interaction and storage. The DSAC electrode material showed the highest specific capacitance values at 630.18 F g^{-1} and 378.85 F g^{-1} at 1 mV s^{-1} and 0.25 A g^{-1} (refer to Tables 4–6) for CV curves and GCD cycles, respectively. These findings align with the observed physiochemical (surface area, pore size, and pore volume) and surface morphological characteristics in the DSAC electrode material (refer to Fig. 5 and **6(a)–(d)** respectively). Table 6 compares DSAC with previously reported supercapacitor electrodes. The DSAC electrode material exhibited superior electrochemical properties including high specific capacitance, specific energy, and power density. These properties surpass those of template-assisted electrode materials from previously reported supercapacitor electrodes in the literature, as summarized in Table 6.

Fig. 9 shows the cycling stability plots at a current density of 1 A g^{-1} for 5000 cycles for all the samples. The cycling plots were obtained by plotting the capacitance values at an interval of 500 up to the 5000th cycle. The stability test was conducted by scanning the electrodes at a constant current of 4 mA against an electrode mass of 4 mg. The capacitance retention for CB, ACB, and DSAC electrodes is 86.19%, 91.57%, and 94.29%, respectively, indicating the stability of the electrode materials. The DSAC electrode showed the highest capacitance retention value of 94.29% indicating superior long-term electrochemical stability. The increased stability of DSAC is due to the morphology replication and the traces of elements such as Si, Al, Mg, Fe, and K in the DSAC sample resulting from the diatomite template-assisted method.
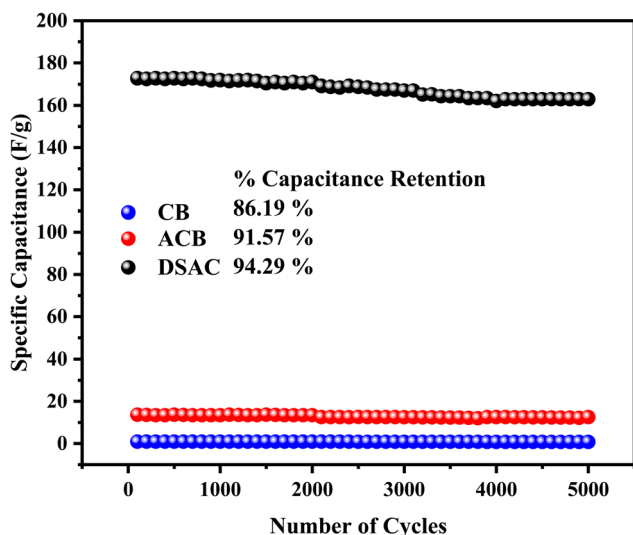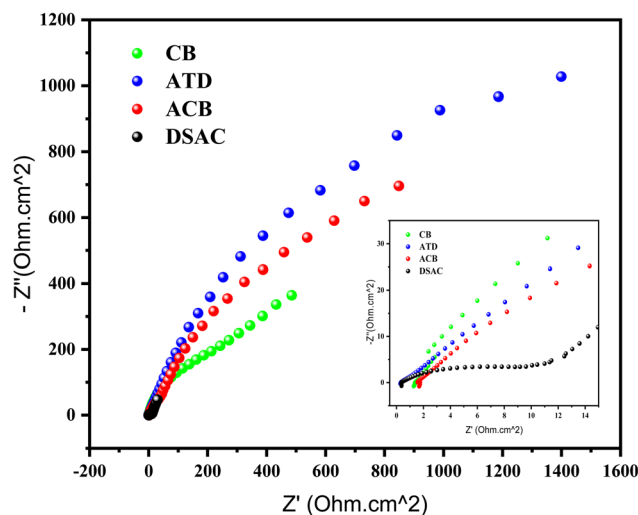

Fig. 10 Nyquist plot of the CB, ATD, ACB, and DSAC samples.

The Nyquist plot of the CB, ATD, ACB, and DSAC samples is shown in Fig. 10. CB, ATD, and ACB samples showed similar Nyquist spectra (knee curve or 45° angle curve) as presented in Fig. 10, indicating a capacitive electrochemical behaviour. The ATD electrode material had the highest spectrum within the elevated frequency area. This is due to the presence of numerous active sites, attributed to the porous nature of the electrode material. However, the DSAC electrode showed quite a different Nyquist spectrum which was very short and only observed at a high frequency. However, from the inset of Fig. 10, the spectra of the DSAC electrode material showed a long semi-circle curve signifying a redox or charge transfer reaction within the pores of the DSAC electrode material. The redox or charge transfer reaction observed in the DSAC Nyquist spectra can also be attributed to the increase in the elemental composition of some elements including Si, K, Fe, O, Al, and Mg as summarized in Table 1. While the DSAC electrode exhibited a low equivalent series resistance (ESR/R_s = 0.377 Ω), its charge transfer resistance (R_{CT}) is notably high at 9 Ω. The electric double layer and pseudocapacitive behaviour observed in the DSAC electrode material contribute to the outstanding electrochemical performance as shown in Figures 7(a), 8(a), 9, and 10, and Tables 4–6 respectively.

4 Conclusion

This study aimed to advance the use of diatomite bio-templated synthesis of porous carbon electrodes from CB for energy storage applications. Herein diatomite synthesized activated carbon (DSAC) from CB with exceptional electrochemical performance was successfully fabricated. Through a comprehensive analysis using various techniques such as X-ray diffraction, Raman spectroscopy, scanning electron microscopy, and electrochemical impedance spectroscopy, the study provided detailed insights into the material's physiochemical and electrochemical properties. Distinctive features were observed in the X-ray diffraction patterns, with DSAC showing

Fig. 9 Cycling stability plot for the CB, ACB, and DSAC electrode samples at a current density of 1 A g^{-1}.

broader and less intense (0 0 2) peaks compared to CB. Moreover, ACB exhibited a decrease in (0 0 2) peak intensity after activation, indicating the emergence of defects or pores. Raman spectroscopy revealed a balanced presence of disordered or amorphous carbon and graphite in all samples, with DSAC showing superior physical properties such as a higher mean pore radius, pore volume, and specific surface area that align well with the hierarchical pore structures in diatomite. DSAC demonstrated outstanding electrochemical performance with a specific capacitance value of 630.18 F g^{-1} and 378.85 F g^{-1} at 1 mV s^{-1} and 0.25 A g^{-1} and an exceptional capacitance retention percentage of 94.29 after 5000 cycles, outperforming CB, ACB, and ATD. DSAC also exhibited significantly lower resistance/impedance values. In summary, the study highlighted that DSAC effectively replicates the hierarchical porous network structure of diatomite, providing desired and controlled porosity, microstructure, and morphology, leading to improved electrochemical performance making it an economically attractive and environmentally friendly candidate for supercapacitor applications.

Data availability

The datasets generated and/or analyzed during the current study are available from the corresponding author upon reasonable request.

Author contributions

Appiah Eugene Sefa: conceptualization, methodology, validation, formal analysis, investigation, resources, writing – original draft. Kwadwo Mensah-Darkwa: conceptualization, resources, writing – review & editing, supervision, validation, funding acquisition. Anthony Andrews: formal analysis, writing – review & editing, supervision, validation. Frank Ofori Agyemang: formal analysis, writing – review & editing, supervision, validation. Martinson Addo Nartey: conceptualization, formal analysis, investigation, resources, writing – review & editing, supervision, validation. Katlego Makgopa: conceptualization, methodology, formal analysis, writing – review & editing, supervision, validation. Yongdan Hou: formal analysis, writing – review & editing, supervision, validation. Patrick Aggrey: formal analysis, investigation, resources, writing – review & editing. David Ato Quansah: formal analysis, writing – review & editing, supervision, validation.

Conflicts of interest

The authors declare no conflict of interest, financial or otherwise.

Acknowledgements

References

1 R. T. Ayinla, J. O. Dennis, H. M. Zaid, Y. K. Sanusi, F. Usman and L. L. Adebayo, A review of technical advances of recent palm bio-waste conversion to activated carbon for energy storage, *J. Cleaner Prod.*, 2019, **229**, 1427–1442, DOI: **10.1016/j.jclepro.2019.04.116**.

2 T. K. Enock, C. K. King'ondu, A. Pogrebnoi and Y. A. C. Jande, Status of Biomass Derived Carbon Materials for Supercapacitor Application, *Int. J. Electrochem.*, 2017, **2017**, 1–14.

3 A. Kasaeian, A. Razmjoo, R. Shirmohammadi, F. Pourfayaz and A. Sumper, Deployment of a stand-alone hybrid renewable energy system in coastal areas as a reliable energy source, *Environ. Prog. Sustainable Energy*, 2020, **39**(3), e13354.

4 D. Assylkhanova, M. Nazhipkyzy, A. Maltay, A. Zhaparova and A. Niyazbaeva, Electrode materials for Li-ion batteries based on diatomite, *Combustion and Plasma Chemistry*, 2022, **20**(3), 191–197.

5 S. Herou, P. Schlee, A. B. Jorge and M. Titirici, Biomass-derived electrodes for flexible supercapacitors, *Curr. Opin. Green Sustainable Chem.*, 2018, **9**, 18–24, DOI: **10.1016/j.cogsc.2017.10.005**.

6 T. Selvaraj, V. Perumal, S. F. Khor, L. S. Anthony, S. C. B. Gopinath and M. N. Muti, The recent development of polysaccharides biomaterials and their performance for supercapacitor applications, *Mater. Res. Bull.*, 2020, **126**(February), 110839, DOI: **10.1016/j.materresbull.2020.110839**.

7 S. Ban, J. Zhang, L. Zhang, K. Tsay, D. Song and X. Zou, Electrochimica Acta Charging and discharging electrochemical supercapacitors in the presence of both parallel leakage process and electrochemical decomposition of solvent, *Electrochim. Acta*, 2013, **90**, 542–549, DOI: **10.1016/j.electacta.2012.12.056**.

8 Y. Lv, L. Li, Y. Zhou, M. Yu, J. Wang, J. Liu, *et al.*, A cellulose-based hybrid 2D material aerogel for a flexible all-solid-state supercapacitor with high specific capacitance, *RSC Adv.*, 2017, **7**(69), 43512–43520.

9 D. P. Dubal, Advances in flexible supercapacitors for portable and wearable smart gadgets, *Emerging Materials for Energy Conversion and Storage*, Elsevier Inc., 2018, pp. 209–246, DOI: **10.1016/B978-0-12-813794-9.00007-7**.

10 J. Jose, V. Thomas, V. Vinod, R. Abraham and S. Abraham, Nanocellulose based functional materials for supercapacitor applications, *J. Sci.: Adv. Mater. Devices*, 2019, **4**(3), 333–340, DOI: **10.1016/j.jsamd.2019.06.003**.

11 Z. Zeng, Y. Dong, S. Yuan, W. Zhao, L. Wang, S. Liu, *et al.*, Natural mineral compounds in energy-storage systems : Development, challenges, prospects, *Energy Storage Mater.*, 2022, **45**, 442–464.

12 M. Sevilla and A. B. Fuertes, Direct synthesis of highly porous interconnected carbon nanosheets and their application as

high-performance supercapacitors, *ACS Nano*, 2014, **8**(5), 5069–5078.

13 W. Zhang, R. R. Cheng, H. H. Bi, Y. H. Lu, L. B. Ma and X. J. He, A review of porous carbons produced by template methods for supercapacitor applications, *N. Carbon Mater.*, 2021, **36**(1), 69–81, DOI: 10.1016/S1872-5805(21)60005-7.

14 L. Wan, J. Hu, J. Liu, M. Xie, Y. Zhang, J. Chen, *et al.*, Heteroatom-doped porous carbons derived from lotus pollen for supercapacitors: Comparison of three activators, *J. Alloys Compd.*, 2021, **859**, 158390.

15 E. E. Miller, Y. Hua and F. H. Tezel, Materials for energy storage: Review of electrode materials and methods of increasing capacitance for supercapacitors, *J. Energy Storage*, 2018, **20**, 30–40.

16 M. I. A. A. Maksoud, R. Amer, F. Ahmed, E. Shalan, M. A. Elkodous, S. O. Olojede, *et al.*, Advanced materials and technologies for supercapacitors used in energy conversion and storage : a review, *Environ. Chem. Lett.*, 2021, **19**, 375–439, DOI: 10.1007/s10311-020-01075-w.

17 M. Nasibi, M. A. Golozar and G. Rashed, Nanoporous carbon black particles as an electrode material for electrochemical double layer capacitors, *Mater. Lett.*, 2013, **91**, 323–325, DOI: 10.1016/j.matlet.2012.09.088.

18 M. Nasibi, M. A. Golozar and G. Rashed, Nano iron oxide (Fe2O3)/carbon black electrodes for electrochemical capacitors, *Mater. Lett.*, 2012, **85**, 40–43, DOI: 10.1016/j.matlet.2012.06.109.

19 C. C. Chen, Y. H. Huang and H. J. Chien, Waste tire-derived porous nitrogen-doped carbon black as an electrode material for supercapacitors, *Sustainable Chem. Pharm.*, 2021, **24**(September), 100535, DOI: 10.1016/j.scp.2021.100535.

20 R. B. González-González, L. T. González, S. Iglesias-González, E. González-González, S. O. Martinez-Chapa, M. Madou, *et al.*, Characterization of chemically activated pyrolytic carbon black derived from waste tires as a candidate for nanomaterial precursor, *Nanomaterials*, 2020, **10**(11), 1–22.

21 M. A. U. Fazara, I. Jainoo, K. N. Ismail, K. Hussin, and M. R. Fahmi, Physicochemical properties of pyrolitic carbon black from waste tyres, in *Key Engineering Materials*, 2014, pp. 178–182.

22 R. Mis-Fernandez, J. A. Azamar-Barrios and C. R. Rios-Soberanis, Characterization of the powder obtained from wasted tires reduced by pyrolysis and thermal shock process, *J. Appl. Res. Technol.*, 2008, **6**(2), 95–105.

23 R. I. Sugatri, Y. C. Wirasadewa, K. E. Saputro, E. Y. Muslih, R. Ikono and M. Nasir, Recycled carbon black from waste of tire industry: thermal study, *Microsyst. Technol.*, 2018, **24**(1), 749–755.

24 G. A. Safitri, K. Nueangnoraj, P. Sreearunothai and J. Manyam, Fabrication of activated carbon pouch cell supercapacitor: Effects of calendering and selection of separator-solvent combination, *Curr. Appl. Sci. Technol.*, 2020, **20**(1), 124–135.

25 L. Wu, Y. Li, Z. Fu and B. L. Su, Hierarchically structured porous materials: Synthesis strategies and applications in energy storage, *Natl. Sci. Rev.*, 2020, **7**, 1667–1701.

26 Y. Liu, J. Chen, B. Cui, P. Yin and C. Zhang, Design and Preparation of Biomass-Derived Carbon Materials for Supercapacitors: A Review, *C*, 2018, **4**(4), 53.

27 V. Pavlenko, H. S. Khosravi, S. Żółtowska, A. B. Haruna, M. Zahid, Z. Mansurov, *et al.*, A comprehensive review of template-assisted porous carbons: Modern preparation methods and advanced applications, *Mater. Sci. Eng., R*, 2022, **149**, 100682.

28 C. Wang, B. Yan, J. Zheng, L. Feng, Z. Chen, Q. Zhang, *et al.*, Recent progress in template-assisted synthesis of porous carbons for supercapacitors, *Adv. Powder Mater.*, 2022, **1**(2), 100018, DOI: 10.1016/j.apmate.2021.11.005.

29 Y. Zhou, X. Ren, Y. Du, Y. Jiang, J. Wan and F. Ma, In-situ template cooperated with urea to construct pectin-derived hierarchical porous carbon with optimized pore structure for supercapacitor, *Electrochim. Acta*, 2020, **355**, 136801.

30 T. Roostaei, M. Reza, H. Zhao and M. Eisapour, Recent advances and progress in biotemplate catalysts for electrochemical energy storage and conversion, *Adv. Colloid Interface Sci.*, 2023, **318**(June), 102958, DOI: 10.1016/j.cis.2023.102958.

31 J. Li, Q. Jiang, L. Wei, L. Zhong and X. Wang, Simple and scalable synthesis of hierarchical porous carbon derived from cornstalk without pith for high capacitance and energy density, *J. Mater. Chem. A*, 2020, **8**(3), 1469–1479.

32 G. P. Pandey, S. A. Klankowski, T. Liu, J. Wu and J. Li, Toward highly stable solid-state unconventional thin-film battery-supercapacitor hybrid devices: Interfacing vertical core-shell array electrodes with a gel polymer electrolyte, *J. Power Sources*, 2017, **342**, 1006–1016.

33 Q. Jian, M. Huang, T. Wang, X. Ying, L. Sun, X. Long, *et al.*, Journal of Colloid and Interface Science Biotemplate derived three dimensional nitrogen doped graphene@MnO2 as bifunctional material for supercapacitor and oxygen reduction reaction catalyst, *J. Colloid Interface Sci.*, 2019, **544**, 155–163, DOI: 10.1016/j.jcis.2019.02.089.

34 P. Aggrey, M. Nartey, Y. Kan, J. Cvjetinovic, A. Andrews, A. I. Salimon, *et al.*, On the diatomite-based nanostructure-preserving material synthesis for energy applications, *RSC Adv.*, 2021, **11**, 31884–31922.

35 M. H. Wu, K. L. Li, X. Y. Zhang, P. Gan, J. L. Ge, D. N. Tian, *et al.*, Tuning Hierarchical Ferric Nanostructures-Decorated Diatomite for Supercapacitors, *Nanoscale Res. Lett.*, 2018, **13**, 4–9.

36 Y. X. Zhang, M. Huang, F. Li, X. L. Wang and Z. Q. Wen, One-pot synthesis of hierarchical MnO2-modified diatomites for electrochemical capacitor electrodes, *J. Power Sources*, 2014, **246**, 449–456.

37 Y. Yang, A. Li, X. Cao, F. Liu, S. Cheng and X. Chuan, Use of a diatomite template to prepare a MoS2/amorphous carbon composite and exploration of its electrochemical properties as a supercapacitor, *RSC Adv.*, 2018, **8**(62), 35672–35680.

38 S. Kang, C. Wang, J. Chen, T. Meng and E. Jiaqiang, Progress on solvo/hydrothermal synthesis and optimization of the

cathode materials of lithium-ion battery, *J. Energy Storage*, 2023, **67**(May), 107515, DOI: 10.1016/j.est.2023.107515.

39 K. Li, X. Liu, T. Zheng, D. Jiang, Z. Zhou and C. Liu, Tuning MnO 2 to FeOOH replicas with bio-template 3D morphology as electrodes for high performance asymmetric supercapacitors, *Chem. Eng. J.*, 2019, **370**(March), 136–147, DOI: 10.1016/j.cej.2019.03.190.

40 Y. Huang, Y. Wang, Y. Cai, H. Wang, Q. Li, Q. Wu, *et al.*, Diatomite waste derived N-doped porous carbon for applications in the oxygen reduction reaction and supercapacitors, *Nanoscale Adv.*, 2021, **3**(13), 3860–3866.

41 X. L. Guo, M. Kuang, F. Li, X. Y. Liu, Y. X. Zhang, F. Dong, *et al.*, Engineering of three dimensional (3D) diatom@TiO2@MnO2 composites with enhanced supercapacitor performance, *Electrochim. Acta*, 2016, **190**, 159–167.

42 J. Lee, Y. A. Lee, C. Y. Yoo, J. J. Yoo, R. Gwak, W. K. Cho, *et al.*, Self-templated synthesis of interconnected porous carbon nanosheets with controllable pore size: Mechanism and electrochemical capacitor application, *Microporous Mesoporous Mater.*, 2018, **261**, 119–125, DOI: 10.1016/j.micromeso.2017.10.047.

43 N. M. Nanzumani, F. O. Agyemang, K. Mensah-Darkwa, E. S. Appiah, E. K. Arthur, E. Gikunoo, *et al.*, Molten salt synthesis of nitrogen-doped hierarchical porous carbon from plantain peels for high-performance supercapacitor, *J. Electroanal. Chem.*, 2022, **920**(April), 116645, DOI: 10.1016/j.jelechem.2022.116645.

44 L. Pang, B. Zou, Y. Zou, X. Han, L. Cao, W. Wang, *et al.*, Colloids and Surfaces A : Physicochemical and Engineering Aspects A new route for the fabrication of corn starch-based porous carbon as electrochemical supercapacitor electrode material, *Colloids Surf., A*, 2016, **504**, 26–33, DOI: 10.1016/j.colsurfa.2016.05.049.

45 P. Sharma and V. Kumar, A Brief Review on Supercapacitor, *Pramana Research Journal*, 2018, **8**(3), 50–55.

46 S. Balasubramaniam, A. Mohanty and S. K. Balasingam, Comprehensive Insight into the Mechanism , Material Selection and Performance Evaluation of Supercapatteries, *Nano-Micro Lett.*, 2020, **12**, 1–46, DOI: 10.1007/s40820-020-0413-7.

47 Y. Wang, Y. Song and Y. Xia, Electrochemical capacitors: Mechanism, materials, systems, characterization and applications, *Chem. Soc. Rev.*, 2016, **45**, 5925–5950.

48 C. Ozdemir, O. Y. Gumus, G. Calis-Ismetoglu and H. I. Unal, Electroactively smart vibration damping suspensions of diatomite/silicone oil, *Rheol. Acta*, 2022, **61**(7), 459–472, DOI: 10.1007/s00397-022-01342-3.

49 M. Boota, M. P. Paranthaman, A. K. Naskar, Y. Li, K. Akato and Y. Gogotsi, Waste tire derived carbon-polymer composite paper as pseudocapacitive electrode with long cycle life, *ChemSusChem*, 2015, **8**(21), 3576–3581.

50 G. A. M. Ali, M. M. Yusoff and K. F. Chong, Graphene: Electrochemical production and its energy storage properties, *ARPN J. Eng. Appl. Sci.*, 2016, **11**(16), 9712–9717.

51 R. Kumar, T. Bhuvana and A. Sharma, Tire Waste Derived Turbostratic Carbon as an Electrode for a Vanadium Redox Flow Battery, *ACS Sustain. Chem. Eng.*, 2018, **6**(7), 8238–8246.

52 M. Yu, Y. Han, J. Li and L. Wang, International Journal of Biological Macromolecules Magnetic N-doped carbon aerogel from sodium carboxymethyl cellulose/collagen composite aerogel for dye adsorption and electrochemical supercapacitor, *Int. J. Biol. Macromol.*, 2018, **115**, 185–193, DOI: 10.1016/j.ijbiomac.2018.04.012.

53 M. Ren, C. Y. Zhang, W. Y. lin and J. jun Cai, Development of N-doped carbons from zeolite-templating route as potential electrode materials for symmetric supercapacitors, *Int. J. Miner., Metall. Mater.*, 2018, **25**(12), 1482–1492.

54 K. Li, Z. Hu, R. Zhao, J. Zhou, C. Jing, Q. Sun, *et al.*, A multidimensional rational design of nickel–iron sulfide and carbon nanotubes on diatomite *via* synergistic modulation strategy for supercapacitors, *J. Colloid Interface Sci.*, 2021, **603**, 799–809, DOI: 10.1016/j.jcis.2021.06.131.